

Aurélië CHAMPAGNE

Institute of Condensed Matter and Nanosciences,
 Université catholique de Louvain, Chemin des Etoiles 8,
 B-1348 Louvain-la-Neuve, Belgium
 aurelie.champagne@uclouvain.be
 +32 (0) 10 47 85 66



Insights into the physical properties of the MAX phases and MXenes: from experiments to first-principles modeling

1. Introduction and objectives

This article reports the main results obtained during my PhD thesis which was conducted under the supervision of Prof. Jean-Christophe Charlier. The materials studied herein include the three-dimensional (3D) MAX phases and their two-dimensional (2D) derivatives, MXenes.

The MAX phases are layered hexagonal 3D solids composed of 2D $M_{n+1}X_n$ sheets separated by A layer [1], thus exhibiting a general formula $M_{n+1}AX_n$, where M represents an early transition metal, A is an element from groups 13 to 16, X is either C or N atom, and n varies from 1 to 3

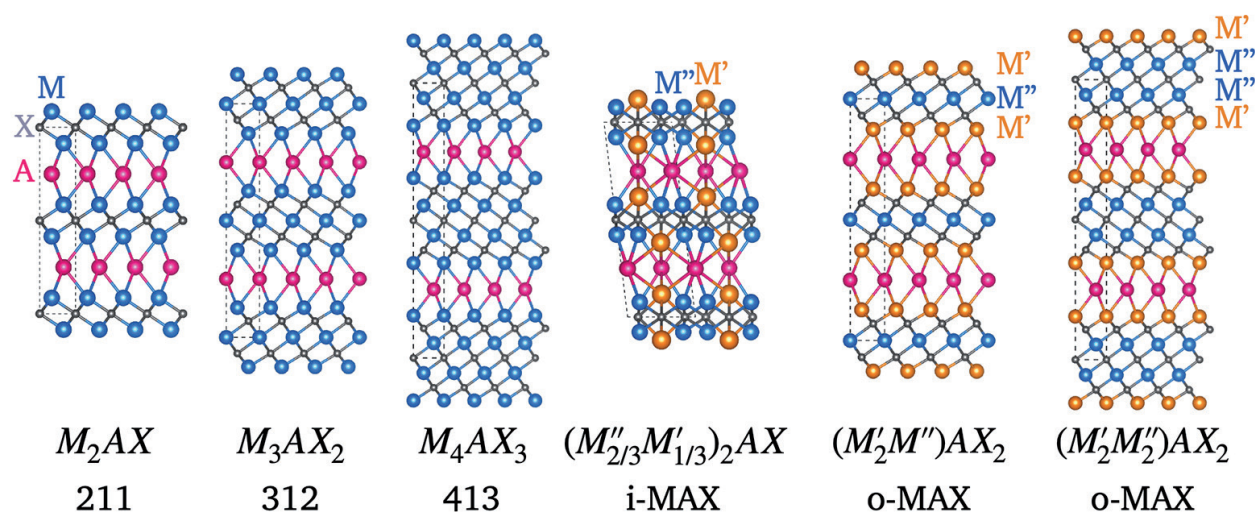


Figure 1. Atomic structure of existing MAX phases, including ternary $M_{n+1}AX_n$ ($n = 1, 2, 3$) phases, and quaternary in-plane ordered (i-MAX) and out-of-plane ordered (o-MAX) phases. The unit cells are represented with dashed lines and the M, A, and X elements are respectively represented by small blue/orange, pink, and gray spheres.

[1]. Depending on their n value, the MAX phases can be categorized as 211 phases for M_2AX , 312 phases for M_3AX_2 , and 413 phases for M_4AX_3 (Figure 1). The main difference between the structures of the 211, 312, and 413 phases is the number of M layers separating the A layers.

The MXenes are 2D transition metal carbides or nitrides obtained from the selective etching of A layers from the parent 3D MAX phases [2]. Since the etching process is often performed in hydrofluoric acid (HF) solution, MXenes have a general formula $M_{n+1}X_nT_z$ ($n = 1, 2, 3$) where T_z are termination groups such as $-F$, $-OH$, or $=O$, mostly depending on the nature of the chemical environment [3].

This work had four main objectives. The first one was to investigate both experimentally and theoretically the electrical, vibrational, thermal, and elastic properties of the 3D MAX phase single crystals and the potential anisotropy thereof.

In particular, Cr_2AlC single crystals were studied (Figure 2(a)). The second goal involved the study of the recently discovered rare-earth (RE) containing MAX phases, coined RE-i-MAX, and the experimental characterization of monocrystalline samples (Figure 2(b)). As a third goal, the potential exfoliation of 3D MAX phases into their 2D counterparts, MXenes, was predicted theoretically. Eventually, the fourth goal concerned the 2D MXene systems, in particular the V_2CT_z ones (Figure 2(c)). It consisted in the investigation of their structural, electronic, and vibrational properties, including the establishment of their Raman fingerprint.

Most of the research projects carried out as part of this thesis consisted in both theoretical and experimental studies and involved close collaborations with different experimental groups, in particular those of M. W. Barsoum (Drexel University, USA), T. Ouisse (LMGP Grenoble, France), and J. Rosen (Linköping University, Sweden). First-

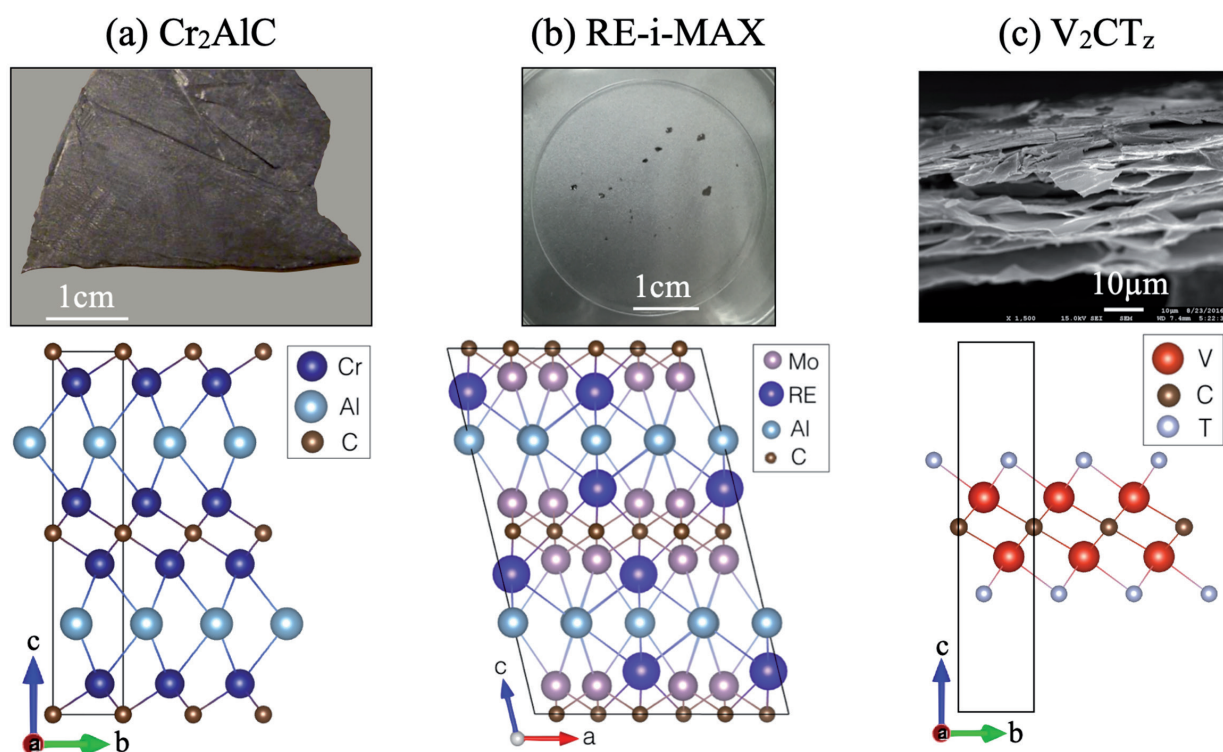


Figure 2. Materials investigated in this thesis, including 3D MAX phase single crystals: (a) Cr_2AlC and (b) RE-i-MAX, and 2D MXenes: (c) V_2CT_z .

principles calculations were usually performed within the Abinit or VASP package, using the generalized gradient approximation with norm-conserving or PAW pseudopotentials. For more information, please refer to our previous works.

Since both MAX phases and MXenes are relatively new compounds, the background and literature survey of their synthesis, structures, and properties are introduced in Sections 2 and 3, respectively. The physical properties of the ternary Cr_2AlC system are explored in Section 4, those of RE-i-MAX phases in Section 5, and those of 2D V_2CT_z systems in Section 6. Conclusions are drawn in Section 7.

2. An introduction to MAX phases

2.1. History of the MAX phases

The MAX phases have two histories [4]. The first one started in the early-1960s, when the group of Nowotny in Vienna synthesized a series of ternary carbides and nitrides including about 30 phases with the M_2AX chemistry [5]. At that time, these phases were called 'H-phases'. In 1967, Nowotny's group synthesized the first two 312 phases, Ti_3SiC_2 [6] and Ti_3GeC_2 [7], with similar layered structures than the H-phases. In the early-1990s, the same group reported the synthesis of Ti_3AlC_2 [8–10].

Subsequently, these phases remained totally unexplored until the mid-1990s - beginning of the second history of the MAX phases - when Barsoum and El-Raghy synthesized fully dense single-phase Ti_3SiC_2 and revealed its outstanding combination of metallic and ceramic-like properties [11, 12]. The compound was light, relatively soft, and readily machinable, was a good electrical and thermal conductor, and was impressively resistant to thermal shock and oxidation up to 1400°C. In 1999, Barsoum and El-Raghy synthesized the first 413 phase, Ti_4AlN_3 [13, 14], and agreed that all 211, 312, and 413 phases form a large family of layered compounds with the general formula $\text{M}_{n+1}\text{AX}_n$ (Figure 1). Today, these phases are commonly referred to as the MAX phases [1].

2.2. Synthesis of the MAX phases

These last two decades, substantial efforts have been made on the synthesis of MAX phases. Initially, all MAX phases were synthesized in powders, bulk materials, or thin films, corresponding to highly polycrystalline forms. In 2011, Mercier and coworkers [15, 16] reported for the first time on a solution growth process to produce MAX single crystals, opening the door to a more accurate characterization of the intrinsic MAX phase properties and their anisotropy.

2.3. Structure and variety of MAX phases

So far about 85 ternary MAX carbides and nitrides have been reported, with eleven different elements on the M sites (Sc, Ti, V, Cr, Mn, Zr, Nb, Mo, Hf, Ta, Lu) and fifteen elements on the A sites (Al, Si, P, S, Zn, Ga, Ge, As, Cd, In, Sn, Ir, Au, Tl, Pb).

Recently, a new route to increase the elemental combination of MAX phases and to optimize their performance was proposed, consisting in the addition of a fourth element, by alloying on the M, A, or X sites [17–19]. Historically, most quaternary MAX phases existed as random solid solutions [19].

In 2014, out-of-plane ordered quaternary MAX phases (o-MAX) were discovered [20], with the general formula $\text{M}'_2\text{M}''\text{AX}_2$ for 312 phases and $\text{M}'_2\text{M}''_2\text{AX}_3$ for 413 phases, where M' and M'' are two different early transition metals. As depicted in Figure 1, two M' layers sandwich either one or two layers of M'' elements. Since 2014, six different o-MAX phases have been synthesized [20–23].

In 2017, in-plane ordered quaternary MAX phases (i-MAX) were theoretically predicted and successfully synthesized with the general formula $(\text{M}''_{2/3}\text{M}'_{1/3})_2\text{AlC}$, where M' and M'' are two different transition metals [24]. As depicted in Figure 1, the two M' and M'' elements are in-plane ordered with the $\text{M}'':\text{M}'$ ratio equal to 2. A requirement for formation of i-MAX phases is a large difference in atomic size between M'

and M' elements which allows for the formation of a M' honeycomb lattice with the M' atoms at the centers of the hexagons [25]. To minimize in-plane stress, the larger M' atoms are displaced toward the Al-layer in which the Al atoms redistribute into a Kagome-like lattice [25]. Since the first report of an i-MAX phase [24], eleven other i-MAX phases were synthesized [23, 25–29]. Interestingly, this ordering allowed the addition of non-traditional MAX phase elements, such as Sc, Y, and W. Very recently, the existence of RE-containing i-MAX phases, RE-i-MAX, with the general formula $(\text{Mo}_{2/3}\text{RE}_{1/3})_2\text{AC}$ (A = Al or Ga), was revealed [30, 31]. Because of their magnetic properties [30, 32], these new phases are expected to attract much attention from the scientific community.

In total, considering both ternary and quaternary MAX phases, as well as solid solution compounds, there are more than 155 different compositions that have been reported experimentally [33]. The MAX phase periodic table of M, A, and X elements is presented in Figure 3 and

highlights the remarkably wide space available to play on the MAX composition and, consequently, on their properties.

2.4. Properties of MAX phases and derived applications

By now, it is well established that at least a subset of MAX phases combines some of the best properties of metals and ceramics [1, 4, 34], including high electrical and thermal conductivities, chemical, oxidation, and thermal shock resistances, as well as reversible deformation [35]. Some of them are discussed hereafter.

The best characterized ternaries to date are Ti_3SiC_2 , Ti_3AlC_2 , and Ti_2AlC . Their transport properties have been intensively studied, including electrical and thermal conductivities and optical and magnetic characteristics. In addition, their elastic and mechanical properties have also been quantified [4]. In contrast to the ternary phases, the quaternary o-MAX and i-MAX phases still

$M_{n+1}AX_n$

1 H Hydrogen 1.008	2 He Helium 4.002602																						
3 Li Lithium 6.94	4 Be Beryllium 9.012182																	5 B Boron 10.81	6 C Carbon 12.011	7 N Nitrogen 14.0064	8 O Oxygen 15.999	9 F Fluorine 18.99840323	10 Ne Neon 20.1797
11 Na Sodium 22.98976928	12 Mg Magnesium 24.305																	13 Al Aluminum 26.9815386	14 Si Silicon 28.0855	15 P Phosphorus 30.973762	16 S Sulfur 32.06	17 Cl Chlorine 35.45	18 Ar Argon 39.948
19 K Potassium 39.0983	20 Ca Calcium 40.078	21 Sc Scandium 44.955912	22 Ti Titanium 47.88	23 V Vanadium 50.9415	24 Cr Chromium 51.9961	25 Mn Manganese 54.938045	26 Fe Iron 55.845	27 Co Cobalt 58.933194	28 Ni Nickel 58.6934	29 Cu Copper 63.546	30 Zn Zinc 65.38	31 Ga Gallium 69.723	32 Ge Germanium 72.630	33 As Arsenic 74.9216	34 Se Selenium 78.9718	35 Br Bromine 79.904	36 Kr Krypton 83.798						
37 Rb Rubidium 85.4678	38 Sr Strontium 87.62	39 Y Yttrium 88.90584	40 Zr Zirconium 91.224	41 Nb Niobium 92.90638	42 Mo Molybdenum 95.94	43 Tc Technetium (98)	44 Ru Ruthenium 101.07	45 Rh Rhodium 102.90550	46 Pd Palladium 106.363	47 Ag Silver 107.8682	48 Cd Cadmium 112.411	49 In Indium 114.818	50 Sn Tin 118.710	51 Sb Antimony 121.757	52 Te Tellurium 127.60	53 I Iodine 126.90447	54 Xe Xenon 131.29						
55 Cs Cesium 132.90545196	56 Ba Barium 137.327	57-71 Lanthanoids	72 Hf Hafnium 178.49	73 Ta Tantalum 180.94788	74 W Tungsten 183.84	75 Re Rhenium 186.207	76 Os Osmium 190.23	77 Ir Iridium 192.222	78 Pt Platinum 195.084	79 Au Gold 196.966569	80 Hg Mercury 200.592	81 Tl Thallium 204.3833	82 Pb Lead 207.2	83 Bi Bismuth 208.9804	84 Po Polonium (209)	85 At Astatine (210)	86 Rn Radon (222)						
87 Fr Francium (223)	88 Ra Radium (226)	89-103 Actinoids	104 Rf Rutherfordium (261)	105 Db Dubnium (268)	106 Sg Seaborgium (266)	107 Bh Bohrium (270)	108 Hs Hassium (269)	109 Mt Meitnerium (278)	110 Ds Darmstadtium (281)	111 Rg Roentgenium (282)	112 Cn Copernicium (285)	113 Nh Nihonium (286)	114 Fl Flerovium (289)	115 Mc Moscovium (288)	116 Lv Livermorium (293)	117 Ts Tennessine (294)	118 Og Oganesson (294)						
57 La Lanthanum 138.90547	58 Ce Cerium 140.12	59 Pr Praseodymium 140.90766	60 Nd Neodymium 144.242	61 Pm Promethium (145)	62 Sm Samarium 150.36	63 Eu Europium 151.964	64 Gd Gadolinium 157.25	65 Tb Terbium 158.92534	66 Dy Dysprosium 162.50014	67 Ho Holmium 164.93033	68 Er Erbium 167.259	69 Tm Thulium 168.93032	70 Yb Ytterbium 173.05448	71 Lu Lutetium 174.967									
89 Ac Actinium (227)	90 Th Thorium 232.0377	91 Pa Protactinium 231.03688	92 U Uranium 238.02891	93 Np Neptunium (237)	94 Pu Plutonium (244)	95 Am Americium (243)	96 Cm Curium (247)	97 Bk Berkelium (247)	98 Cf Californium (251)	99 Es Einsteinium (252)	100 Fm Fermium (257)	101 Md Mendelevium (258)	102 No Nobelium (259)	103 Lr Lawrencium (260)									

Figure 3. Periodic table with all elements experimentally incorporated in ternary and quaternary MAX phases, with M elements highlighted in blue, A elements in pink, and X elements in gray.

await experimental characterization. For the o-MAX phases, only their structures, magnetic ground states, and electrical conductivities have been characterized. For the i-MAX phases, the lack of bulk samples with high-enough purity explains their poor characterization so far.

The MAX phases are all good metal-like conductors, with resistivities ranging from 0.07 to 2 $\mu\Omega\text{m}$ [1, 11, 36] at room temperature (RT) which increase linearly with increasing temperature. In some cases, such as Ti_3SiC_2 and Ti_3AlC_2 , their conductivities are higher than the one of pure Ti metal. Given that the MAX phases are good electrical conductors, it is not too surprising that they have very low Seebeck coefficients [4].

A magnetic ground state has been predicted theoretically and/or observed experimentally for a large number of MAX phases [37, 38]. Almost all magnetic MAX phases contain Cr and/or Mn elements. The latest additions to the list of magnetic MAX phases concern the in-plane ordered $(\text{M}_{2/3}\text{Sc}_{1/3})_2\text{AlC}$ ($\text{M} = \text{Cr}, \text{Mn}$) [29] and $(\text{Mo}_{2/3}\text{RE}_{1/3})_2\text{AlC}$ [30, 31] MAX phases, with various magnetic characteristics.

Similar to the MX binaries, a subset of MAX phases are elastically stiff with Young's and shear moduli in the order of 350 and 150 GPa, respectively [4, 39, 40]. In contrast to the MX binaries, the MAX phases are relatively soft, with Vickers hardness values ranging from 2 to 10 GPa, and are impressively readily machinable. This makes the most noticeable difference between the MAX phases and all the other stiff ceramic compounds. Additionally, they are damage-tolerant and their good mechanical properties are preserved even at high temperature $> 1000^\circ\text{C}$ [34].

Thermally, the MAX phases are all good thermal conductors, for the most part because they are good electrical conductors, with RT thermal conductivities ranging from 12 to 60 $\text{Wm}^{-1}\text{K}^{-1}$ [4]. In addition, the MAX phases are thermal-shock resistant and are quite refractory, making them good candidates for high-temperature applications.

Regarding the oxidation resistance of the MAX

phases, they do not all behave in the same way, since the nature of the oxides that form mostly depends on the MAX composition. To be used in high-temperature applications, this oxide layer should be protective enough up to high temperature and not degrade with time. In this regard, the most promising MAX phases are the Al-containing ones that form a dense protective alumina ($\alpha\text{-Al}_2\text{O}_3$) layer [41–47].

To summarize, the MAX phases have been considered for numerous applications. For instance, their good electrical and thermal properties make them good candidates in electrical contacts, sensors, connectors, *etc.* Additionally, owing to their excellent mechanical properties, some of the MAX phases find applications in micro-mechanical systems, protective coatings, and even in daily-life applications such as non-sticky pans and drilling tools. Finally, their excellent high-temperature properties and oxidation resistance make them promising candidates for high-temperature structural and non-structural applications, including heating elements and gas burning applications [4].

3. An introduction to MXenes

Since the exfoliation of graphene in 2004 and the characterization of its outstanding properties [48, 49], 2D materials have received considerable attention in the field of materials science and device processing. Following the technique initially used to isolate a monolayer graphene from its 3D counterpart, graphite, most 2D materials were obtained from the mechanical exfoliation of a parent 3D phase. This was feasible thanks to the weak van der Waals interlayer interactions intrinsically present in the parent phases.

3.1. Discovery of MXenes

In 2011, Naguib and coworkers [2] showed that 3D nano-laminate MAX phases with strong interlayer bonds could also be exfoliated into 2D crystals, using a combination of chemical etching and sonication techniques. In the initial work [2], a Ti_3AlC_2 powder sample was immersed in

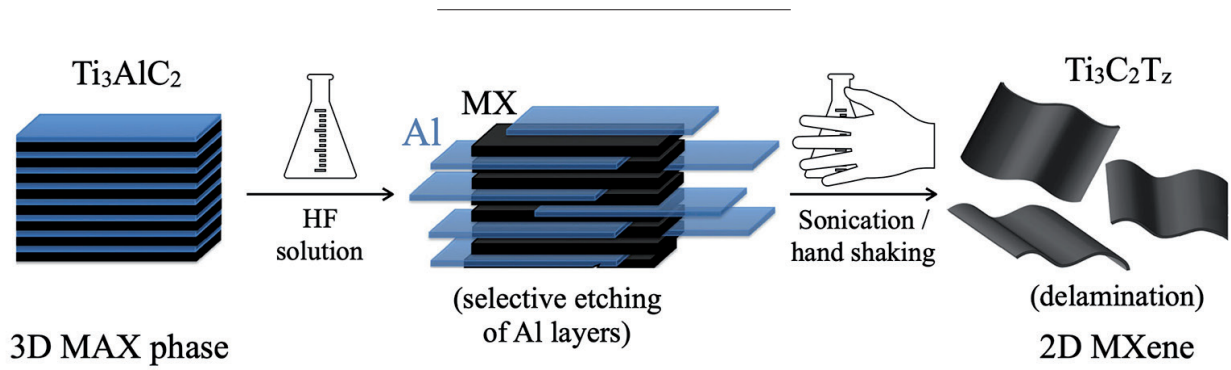


Figure 4. Schematic representation of the synthesis process of 2D MXenes, obtained from the selective etching of the Al planes from the parent 3D MAX phases when immersed in HF solution. Adapted from [50].

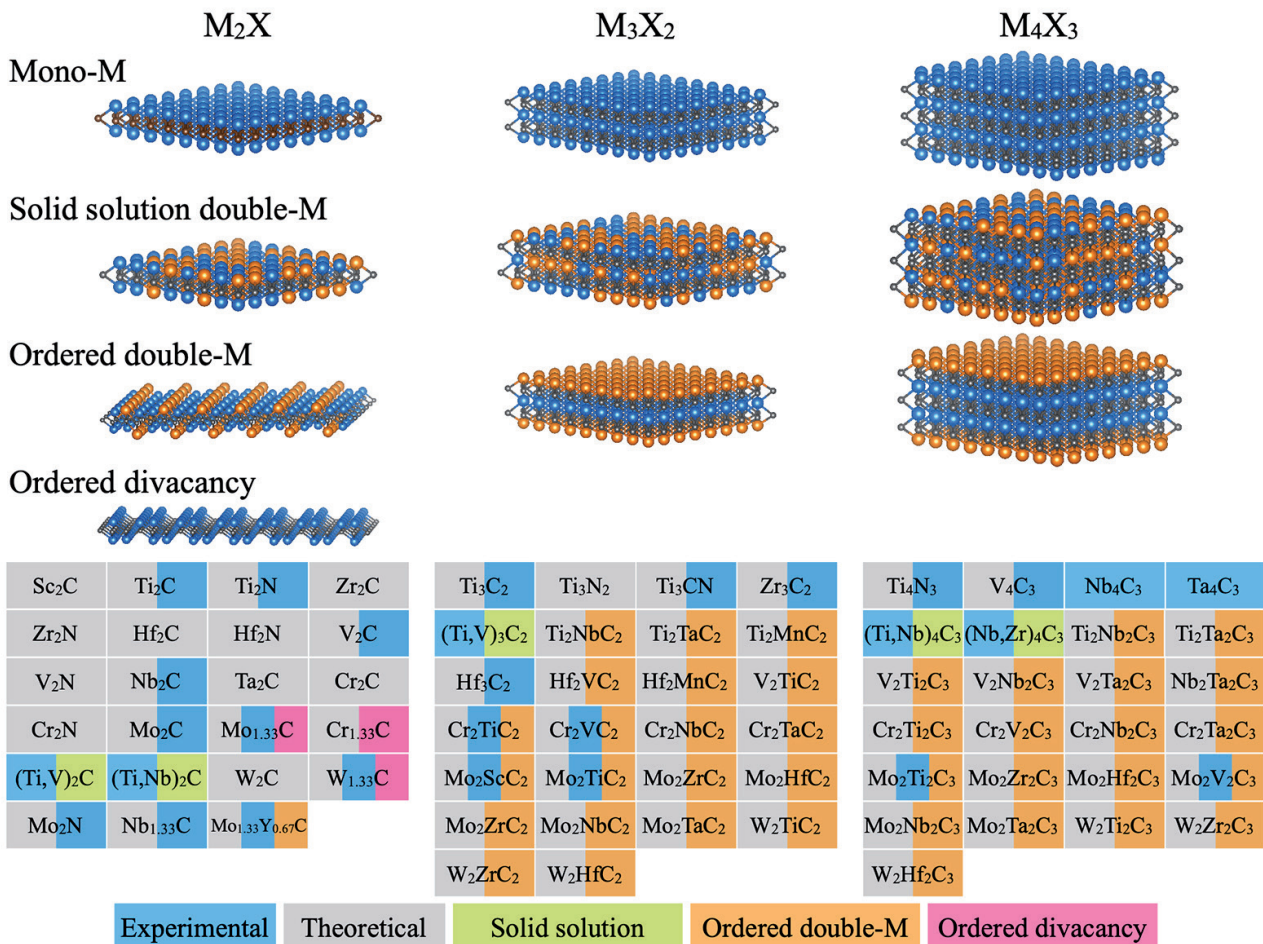


Figure 5. Chemical versatility of all existing MXene systems, including conventional $M_{n+1}X_n$ ($n = 1, 2, 3$), double-M solid solutions, out-of-plane ordered, in-plane ordered double-M, and divacancy ordered $M_{n+1}X_n$ MXene systems. M and X elements are respectively represented by blue/orange and gray small spheres. Adapted from [51].

a 50wt.% concentrated hydrofluoric acid (HF) solution for 2h at RT, resulting in the selective etching of Al planes (Figure 4). This successful etching of a strongly-bonded layered compound represented a major breakthrough in the synthesis of novel 2D systems.

Since then, about 30 transition-metal carbides and nitrides, called MXenes, with different chemical compositions and orders have been reported [3, 50, 51] and up to 70 compositions have been predicted theoretically (Figure 5) [51, 52]. Depending on the 3D precursor, MXenes materials exhibit the formula $M_{n+1}X_nT_z$ ($n = 1, 2, 3$) or $M_{1.33}XT_z$, where M is an early transition metal, X represents either C or N atom, and T_z are termination groups such as $-F$, $-OH$, or $=\overset{\ominus}{O}$, mostly depending on the nature of the chemical environment [3]. The thickness of the MXene monolayer is about 1 nm and varies with the value of the n index and the nature of the terminal groups [51].

3.2. Structure, versatility, and stability of MXenes

The chemical variety of the MAX phases, with over 155 compositions reported so far [1, 33], explains the resulting chemical versatility in 2D MXenes. Since most of the newly discovered MAX phases are Al-based, the family of 2D MXenes is expected to further expand in the near future. To date, a few o-MAX phases have already been exfoliated to form out-of-plane ordered double transition metal MXenes [22, 23] (Figure 5). More interestingly, depending on the etching conditions, the i-MAX phases can be exfoliated to form two different types of MXenes. In-plane ordered double transition metal MXenes are obtained from the selective etching of the Al layers in the parent MAX phase [53], while ordered divacancy MXenes result from the removal of the minority M' element together with the Al element [23, 24] (Figure 5).

The structure of pristine MXenes can be constructed by removing the A element from the parent MAX phases. The atoms are arranged in a layered structure where the X layers are alternatively sandwiched between the M layers (Figure 5). In o-MXenes, the outer-layers are formed with the

M' element, while the inner-layer(s) consist(s) of M'' element. The exfoliation of the i-MAX phases results either in 2D i-MXenes with the general formula $(M''_{2/3}M'_{1/3})_2X$, or in 2D $M_{1.33}X$ systems with ordered divacancies.

As expected from the experimental observations, MXenes become thermodynamically more stable upon surface functionalization and the stability is further enhanced for fully-terminated MXenes (full surface coverage with T_z) [52].

3.3. Properties of MXenes and derived applications

Since the discovery of MXenes in 2011, several experimental and theoretical studies have been conducted to shed light on their chemical and physical properties.

Similar to the MAX phases, the pristine MXenes are predicted to be metallic. Upon functionalization, the electronic properties of MXenes vary from metallic to semiconducting, depending on the nature of the M, X, and T groups [52, 54]. While the majority of terminated MXenes retain their metallic character, some of them are predicted to be semiconductors, due to a shift of the Fermi level [52, 55, 56]. Computed electronic band gaps are summarized in Ref. [57] and range from 0.25 to 3.9 eV. Interestingly, some MXenes (and o-MXenes) with group VI transition metals (Cr, Mo, W) are predicted to be 2D topological insulators, *i.e.*, to present an insulating gap in the bulk and gapless states at the edges. In these systems, the spin-orbit coupling is found to significantly affect the electronic properties.

The magnetic properties of MXenes have been intensively studied from first-principles calculations. Although the majority of the pristine MXenes are non-magnetic, some of them such as Ti_2C , Ti_2N , Cr_2C , Mn_2C , and Mn_2N have ferromagnetic ground-states, while V_2C and Cr_2N are antiferromagnetic. Because of the surface terminations that are inevitably introduced during the synthesis process, none of the magnetic pristine MXenes has been realized in experiment. Interestingly, some functionalized MXenes have been predicted

to preserve a magnetic moment, including Ti_2NO_2 [58], Cr_2NO_2 [59], and all Mn_2CT_2 [60] and Mn_2NT_2 [58] systems, regardless of surface functionalization. Magnetic moments up to $3\mu_B$ have been predicted in these systems that might retain their magnetism up to near RT.

In average, the elastic constants of 2D MXenes are twice larger than those of the corresponding MAX phases [61]. In addition, in most cases, nitrides are stiffer than the carbide counterparts [62]. Further computational studies have investigated the effect of terminations on the elastic properties of MXenes [61, 63]. The presence of terminal groups drastically reduces the elastic constant values of all MXenes. The thickness dependence of the elastic constants has also been studied through first-principles calculations, predicting M_2X systems stiffer than their M_3X_2 and M_4X_3 counterparts [62, 64]. Experimentally, the elastic response of a single layer $\text{Ti}_3\text{C}_2\text{T}_z$ has been measured through nanoindentation technique with an atomic force microscope tip [65]. A Young's modulus of 330 ± 30 GPa was found, which is lower than the one of graphene (1000 ± 100 GPa) and h-BN (870 ± 70 GPa), but is the highest one reported for a solution-processed 2D material [65]. Despite lower Young's modulus than other 2D materials, the higher bending stiffness, hydrophilicity, and high negative zeta potential of MXenes make them promising candidates in composites with polymers, oxides, or carbon nanotubes.

Eventually, 2D MXenes have shown great promise in energy storage applications, which can be explained by their high electronic conductivity, redox active surface generated during the etching process, and 2D morphology optimal for fast ion transport and intercalation [66]. To date, about 50% of the publications on MXenes are on energy-related topics and mostly include experimental works.

Even though energy storage has been the first and most studied application for MXenes, there are several other applications where MXenes have shown great promise, such as transparent conductive electrodes [67, 68], electromagnetic interference shielding [69], hydrogen storage media

[70–73], gas sensors and membranes [74–76], thermoelectric materials [77–80], structural composites [81], catalysts [82–85], organic photovoltaics [86], flexible photovoltaics [87], and many more.

4. Investigation of Cr_2AlC single crystals

Although the MAX phases have been around for more than 20 years [8], the lack of large single crystals has long prohibited a direct assessment of the anisotropy of the physical properties expected from their crystal structure. As a consequence, most of the works on electrical and thermal transport in MAX phases were performed on polycrystals [40, 88]. Since 2011, macroscopic single crystals are available [15, 89, 90], and some of their magneto-transport properties have been investigated [91, 92], as well as their electronic structure [93]. However, given the large diversity in the MAX phase composition, the current amount of experimental measurements performed on single crystal flakes is relatively low.

In this context, the first goal of this thesis consisted in the growth and characterization of MAX single crystals, in general, and Cr_2AlC , in particular.

4.1. Structural properties

The conventional Cr_2AlC unit cell includes eight atoms - four Cr, two Al, and two C atoms - and crystallizes in the $P6_3/mmc$ (#194) space group with hexagonal symmetry (Figure 6(a)). Lattice parameters are respectively $a = b = 0.286$ nm and $c = 1.282$ nm.

4.2. Vibrational properties

The investigation of the vibrational properties of Cr_2AlC single crystals included the description of the phonon dispersion spectra using density functional perturbation theory (DFPT) [94–98] calculations and inelastic neutron scattering (INS) measurements. A phonon spectrum can be seen as a representation of all vibrational modes accessible for the system at a given temperature or energy.

The computed phonon spectrum is presented in Figure 6(b) (blue lines) and is in good agreement with the experimental points (red dots) obtained from the recorded INS resonances along specific crystallographic directions. The absence of imaginary frequencies in the phonon spectrum (Figure 6(b)) confirmed the stability of the system. Additionally, the combination of flat dispersion curves along the Γ A, HK, or ML directions (*i.e.*, along the c -axis) with dispersive curves along

the AH, Γ K, Γ M, or LH directions (*i.e.*, in the ab -plane) was an indication of a mode propagation that exclusively takes place in the ab -plane, hence involving the system to behave as a 2D system [99].

4.3. Electronic properties

Similar to all MAX phases, Cr_2AlC exhibits a metallic behavior ensured by the presence of Cr- d orbitals at the Fermi level (Figure 7) [100].

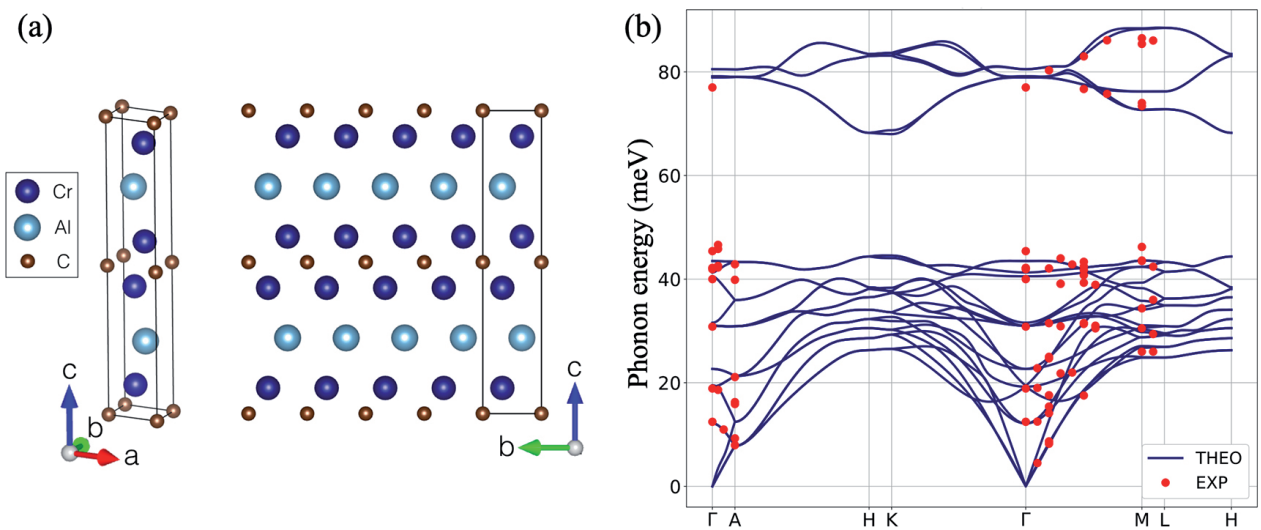


Figure 6. (a) Atomic structure of Cr_2AlC and (b) first-principles phonon spectrum and experimental phonon energy modes of Cr_2AlC along major crystallographic directions.

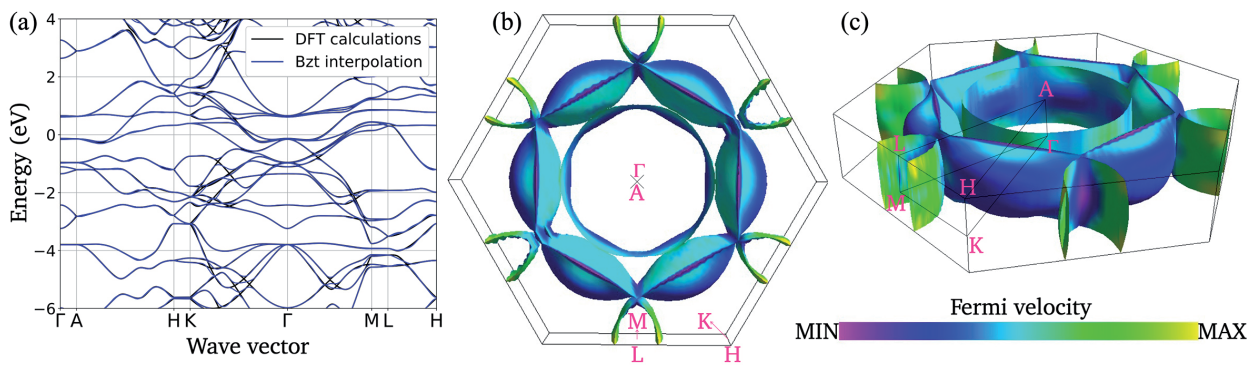


Figure 7. First-principles (a) electronic band structure of Cr_2AlC , with the Fermi level fixed as the reference of zero energy, and (b) and (c) Fermi surfaces computed using the Fermisurfer code [101] and color-coded depending on Fermi velocities.

Experimentally, the electrical conductivity was measured and showed large anisotropy, with the in-plane conductivity about 300 times higher than the out-of-plane one [91]. Theoretically, the anisotropy in the electronic properties can be noticed from the electronic band structure and Fermi surfaces (Figure 7). In Figure 7(a), the dispersive bands along directions parallel to the ab -plane (*i.e.*, AH, Γ K, Γ M, LH) will lead to high carrier velocities and good electronic conductivity in the plane, while the almost flat bands along directions perpendicular to the ab -plane (*i.e.*, Γ A, HK, ML) explain the weak out-of-plane conductivity [100]. Additionally, the open tubular structure of the Fermi surface suggested a quasi 2D character of the Cr_2AlC system [93, 100].

4.4. Thermal transport

The thermal conductivity k can be decomposed into its electronic k_e and lattice k_l contributions, such that $k = k_e + k_l$. The transport theory for electrons is implemented in the BoltzTraP2 code [102, 103] and the estimation of the lattice contribution is achieved using the temperature dependent effective potential (TDEP) code [104–106].

The computed total thermal conductivities are presented in Figure 8. It was observed that both in-plane k_{\parallel} and out-of-plane k_{\perp} thermal conductivities slightly decrease with the temperature. An anisotropy ratio higher than 2 was predicted over the whole temperature range. This anisotropy arises from both the electronic and lattice contributions; the latter being the dominant term [100].

Experimentally, the in-plane and out-of-plane thermal conductivities were measured using, respectively, the modulated photothermal radiometry (MPTR) [107] and the periodic pulse radiometry technique (PPRT) [108]. Experimental curves are presented in Figure 8 and are in the same order of magnitude than our theoretical predictions. As a global observation, the in-plane thermal conductivity was found to be almost constant in the whole temperature range, whereas the out-of-plane thermal conductivity slightly decreased with the temperature and then saturated from 200°C. More importantly, an anisotropy ratio of about 2 was found over the whole temperature range, in agreement with our theoretical results [100].

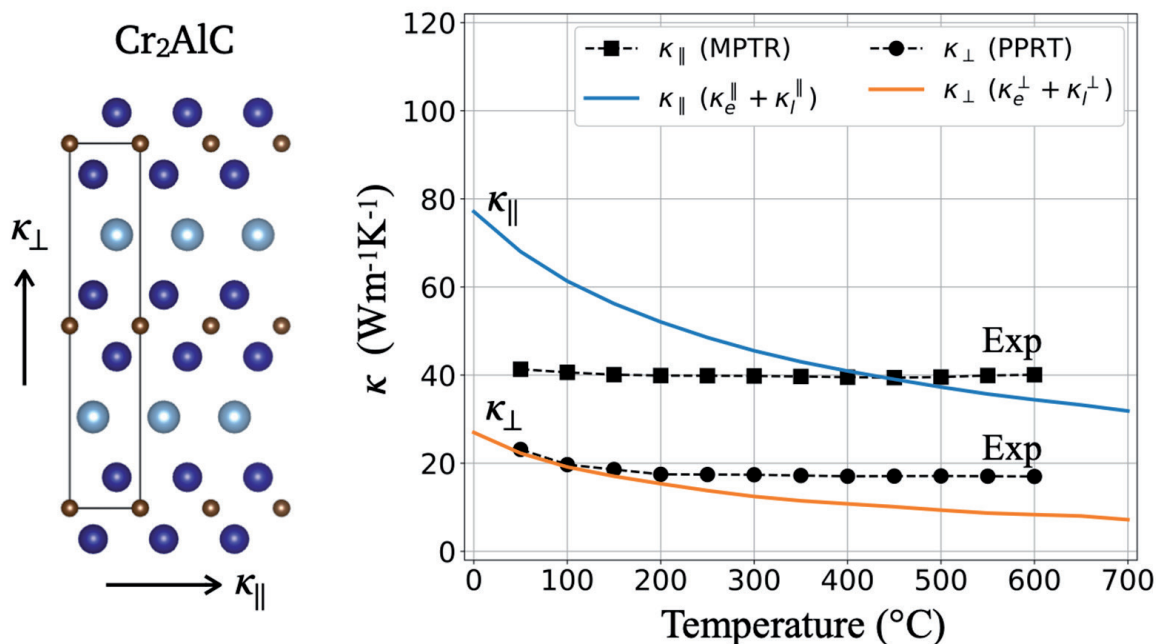


Figure 8. Total thermal conductivity obtained by summing the electronic and lattice contributions: $k = k_e + k_l$, compared to the experimental curves.

4.5. Elastic properties

The last property of Cr_2AlC single crystals that was investigated in the context of this thesis concerns their elastic behavior. For this purpose, the full elastic tensor was computed from first-principles. Additionally, nanoindentation tests were performed allowing for the experimental determination of elastic constants and hardness values.

First-principles calculations provided elastic constants values of $c_{11} = 347$ GPa and $c_{33} = 332$ GPa, respectively along directions parallel and perpendicular to the ab -plane.

Experimentally, 18 indents were performed perpendicularly to the ab -plane while 28 indents were performed parallel to the ab -plane. Representative load-displacement curves for both indentation configurations are depicted in Figure 9(a). Using the Oliver and Pharr method [109, 110], average values of 317 ± 10 GPa and 320 ± 9 GPa were found for c_{11} and c_{33} , respectively. The agreement with the theoretical predictions was remarkable and confirmed the limited anisotropy in the elastic properties [111].

Another fundamental physical parameter that was determined from nanoindentation is the hardness. Using the Oliver and Pharr method [109, 110], the Berkovich hardness of Cr_2AlC single crystal was evaluated to 9.7 ± 0.3 GPa (8.4 ± 0.4 GPa) in a direction perpendicular (parallel) to the ab -plane [111]. The small, but present, anisotropy in the hardness values highlighted the interesting and unique feature of the MAX phases, which respond in an isotropic way to elastic deformation and anisotropically to plastic deformation [112, 113]. This was further evidenced in the scanning electron microscope (SEM) micrographs (Figure 9(b)) where some pileups and delamination cracks are respectively observed upon loading perpendicular and parallel to the basal plane.

4.6. Conclusions

In conclusion, the electronic, vibrational, thermal, and elastic properties of Cr_2AlC single crystals were investigated, combining experimental and theoretical approaches. The anisotropy observed in most physical properties of Cr_2AlC single crystals presumably results from their layered structure. In contrast, the isotropy in the elastic pro-

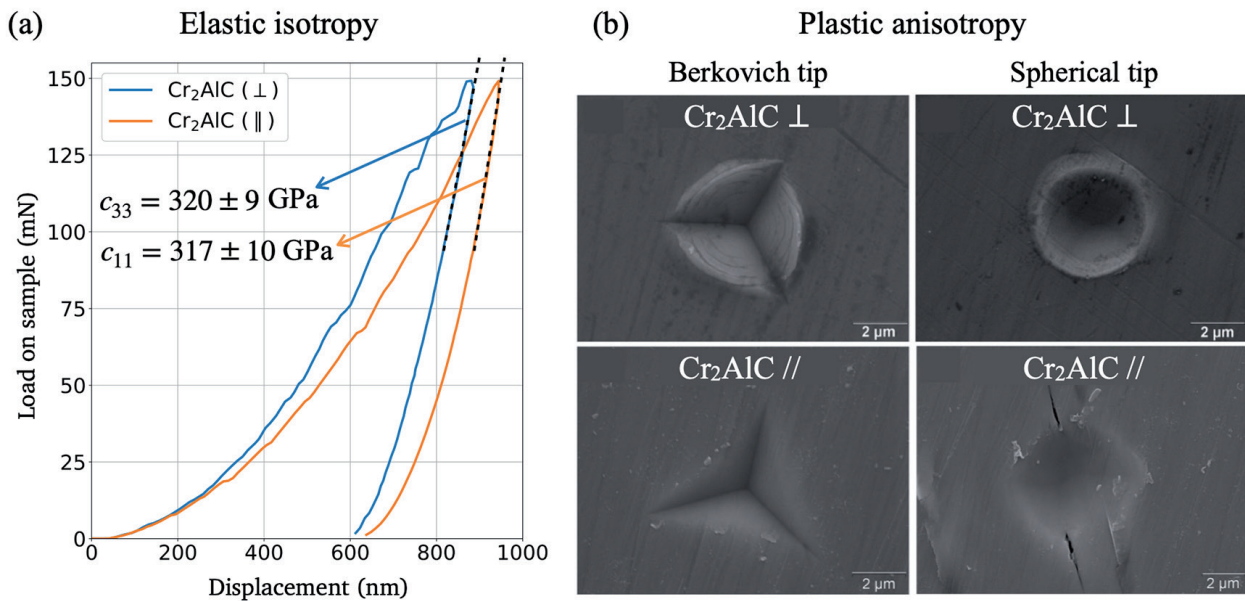


Figure 9. (a) Representative load-displacement curves from the nanoindentation of the top surface and sample side of a Cr_2AlC single crystal and (b) SEM images of the indentation marks of indent performed perpendicularly and parallel to the ab -plane, using a Berkovich or a spherical tip.

properties results from the similar and comparable intra- and inter-layer bonding strengths.

5. Investigation of rare-earth containing MAX phases

Motivated by the recent discovery of RE-i-MAX phases [30, 31] and the possibility to use these magnetic phases as precursor layered compounds to synthesize 2D magnetic MXenes, we investigated their structural, vibrational, elastic, and electronic properties, using both experimental and theoretical approaches.

5.1. Structural properties

The conventional $(\text{Mo}_{2/3}\text{RE}_{1/3})_2\text{AlC}$ unit cell includes 48 atoms - 16 Mo, 8 RE, *i.e.*, Nd, Sm, Gd, Tb, Dy, Ho, Er, Tm, or Lu, 12 Al, and 12 C atoms - and crystallizes in the $C2/c$ (#15) space group. Considering their similar structures, a

schematic representation valid for any RE element is used in Figure 10(a).

The structure and quality of the monocrystalline samples were also investigated using scanning transmission electron microscopy (STEM) [114] (Figure 10(b)). The precise arrangement of the atoms confirmed the $C2/c$ crystalline structure of the system. From the line profile in inset of the second panel, the alternation of one bright RE atom and two less bright Mo atoms is evident. Most of the studied regions were free of faults and only few stacking faults were observed, as the one highlighted by red arrows in the third panel of Figure 10(b).

From the computed and experimental lattice parameters reported in Figure 10(c), it was evident that the increase of the RE atomic mass led to reduced lattice parameters, as expected from the decrease of the covalent atomic radius when moving from left to right on the lanthanide row [115].

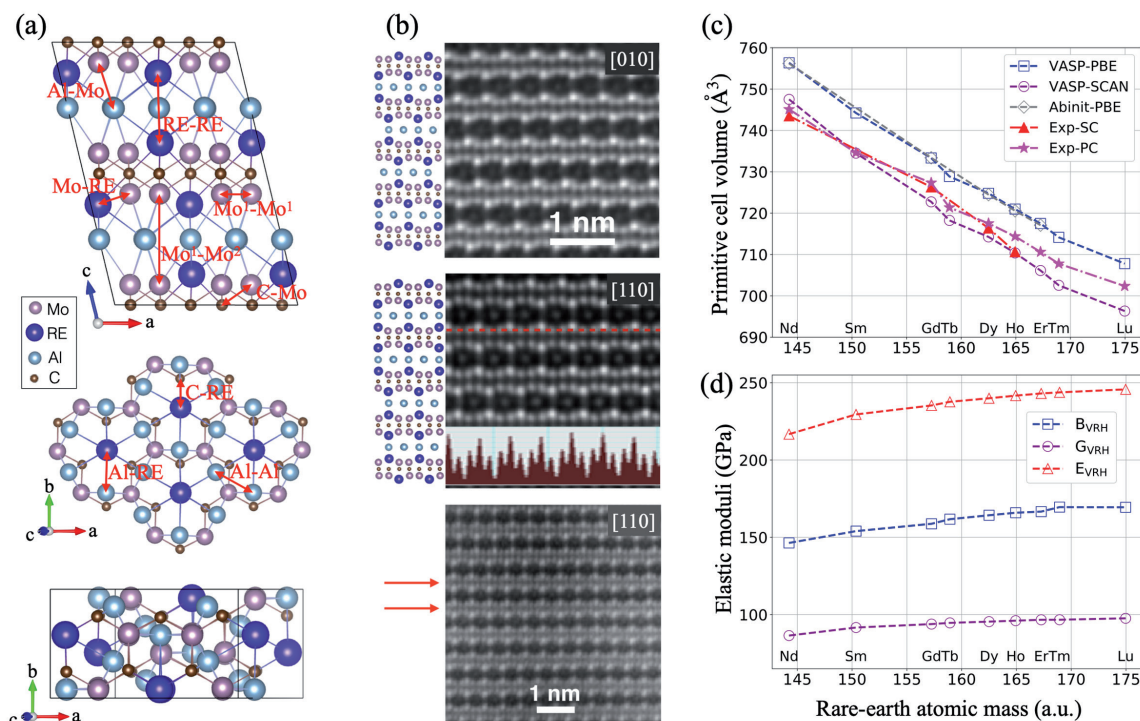


Figure 10. (a) Schematic representation of the conventional monoclinic $C2/c$ cell of $(\text{Mo}_{2/3}\text{RE}_{1/3})_2\text{AlC}$. Some specific interatomic bonds are defined with red arrows. (b) High resolution STEM images for $(\text{Mo}_{2/3}\text{Dy}_{1/3})_2\text{AlC}$ single crystals along $[010]$ and $[110]$ zone axes, with corresponding schematics for the $C2/c$ monoclinic structure. Inset shows line-profile of the Z contrast along the red dashed line while region with stacking fault is pointed out by red arrows. (c) Dependence of the cell volume on RE atomic mass, computed with various first-principles softwares, compared to experimental volumes for single crystals (SC) [114] and polycrystals (PC) [30]. (d) Dependence of computed bulk (B), shear (G), and Young's (E) moduli on RE atomic mass.

5.2. Elastic properties

For all systems, the elastic tensor and homogenized polycrystalline elastic properties including bulk modulus B , shear modulus G , and Young's modulus E were computed from first-principles [116]. The values of the elastic properties presented in Figure 10(d) suggested that an increase of the RE atomic mass, when moving from left to right on the lanthanide row, resulted in an increase of all elastic moduli. In other words, RE-*i*-MAX phases with heavier RE elements are stiffer, which is not too surprising since the unit cell, and hence the atomic bonds, tend to shrink with increasing RE atomic mass (Figure 10(c)).

In addition, the elastic response of a $(\text{Mo}_{2/3}\text{Ho}_{1/3})_2\text{AlC}$ single crystal was measured experimentally using nanoindentation. Using the Oliver and Pharr method [109, 110], the average value of E from 15 indents as was calculated to be 220 ± 8 GPa. In comparison, the computed value was 242 GPa. Once more, the agreement between experimental and theoretical results was remarkable, considering that both defects and temperature were not taken into account in our calculations.

5.3. Exfoliation potential

In previous studies, it has been revealed that not all MAX phases could be etched into their 2D counterparts. In order to avoid losing money in unsuccessful experimental etching, it would be useful to predict beforehand the potential exfoliation of a given MAX phase, using theoretical tools. In this context, given the expensive price of rare-earth elements, ranging from \$50 to \$1,000/kg, we used a theoretical approach to predict the potential exfoliation of RE-*i*-MAX phases.

While the experimental process used to convert MAX phases into MXenes is quite complex, two main criteria, previously exploited by Khazaei and coworkers [116, 117], were used to evaluate their exfoliation potential: (i) bonding strength and (ii) exfoliation energy. For the RE-*i*-MAX to be successfully etched into RE-*i*-MXenes, only the Al bonds, *viz.* Al–Mo and Al–RE, need to be broken (Figure 10(a)). This would only occur if

the C–Mo and C–RE bonds are stronger than the Al–Mo and Al–RE ones.

The computation and analysis of the crystal orbital Hamilton population (COHP) using the Lobster code [118–120] was used to shed light on the nature of the bonding. In particular, by integrating the COHP up to the Fermi level, it was possible to assess the relative bond strengths within the RE-*i*-MAX phases [118–120] (Figure 11(a)). Even though no absolute value for the bond strength could be obtained, the bonds were classified according to their $-\text{IpCOHP}$ curve. From Figure 11(a), the atomic interactions defined in Figure 10(a) were ranked as follows: C–Mo > C–RE > Al–Al > Al–Mo > Al–RE > Mo–Mo \approx Mo–RE. This classification was consistent with the one for conventional MAX phases, where M–X bonds were stronger than M–A bonds (Figure 11(b)) [116, 121], and presumably indicated the exfoliation potential of the RE-*i*-MAX phases [115].

The second criterion is the exfoliation energy E_{exf} which was evaluated as:

$$E_{\text{exf}} = -\frac{E_{\text{tot}}(\text{RE-}i\text{-MAX}) - 2E_{\text{tot}}(\text{RE-}i\text{-MXene}) - 12E_{\text{tot}}(\text{Al})}{4S}$$

where $E_{\text{tot}}(\text{RE-}i\text{-MAX})$, $E_{\text{tot}}(\text{RE-}i\text{-MXene})$, and $E_{\text{tot}}(\text{Al})$ respectively correspond to the ground-state energy of RE-*i*-MAX, RE-*i*-MXene, and bulk aluminum per atom (Figure 12(a)) and S is the surface area determined from the structural parameters. Since no experimental exfoliation data could be found in the literature, the best we could do was compare these theoretical predictions to values for conventional MAX phases, reported by Khazaei *et al.* [116]. Among the successfully etched MAX phases, V_2AlC has the largest theoretical exfoliation energy of 0.205 eV/Å (Figure 12(b)). Therefore, from the computed exfoliation energy values (full markers), we expected that RE-*i*-MAX phases could a priori, be successfully etched into RE-*i*-MXenes.

Combining the analysis of the bonding strength (Figure 11) with the computed exfoliation energy (Figure 12), the exfoliation potential of RE-*i*-MAX phases was predicted [115].

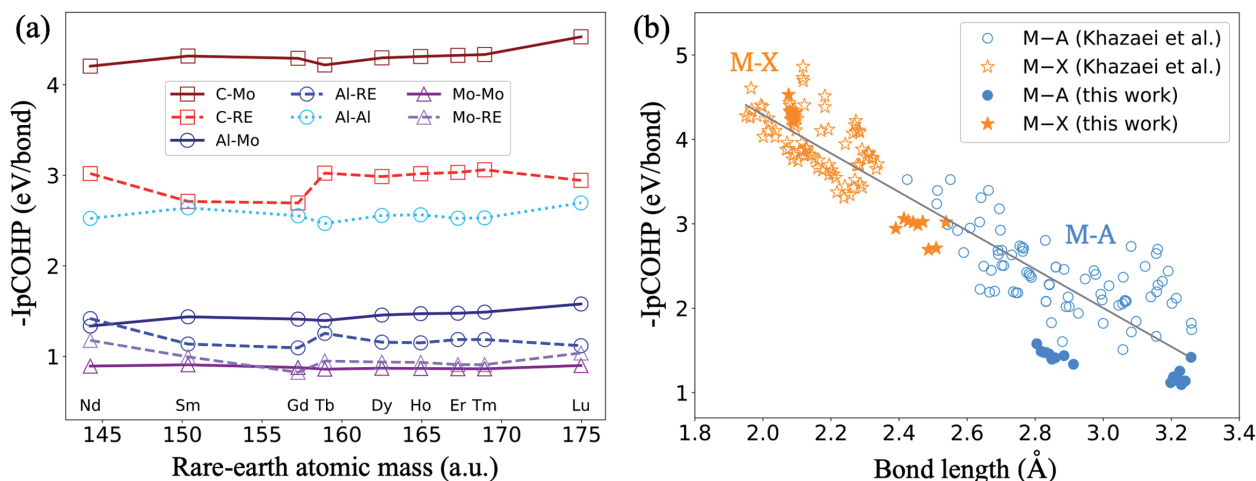


Figure 11. (a) Calculated integrated COHP values at the Fermi level as a function of the RE atomic mass. The relative order of bond strengths is almost unchanged with the RE atomic mass. (b) Integrated COHP for both M-A and M-X bonds for a series of 82 MAX phases (empty markers) [116] plus the 9 considered RE-i-MAX phases (full markers).

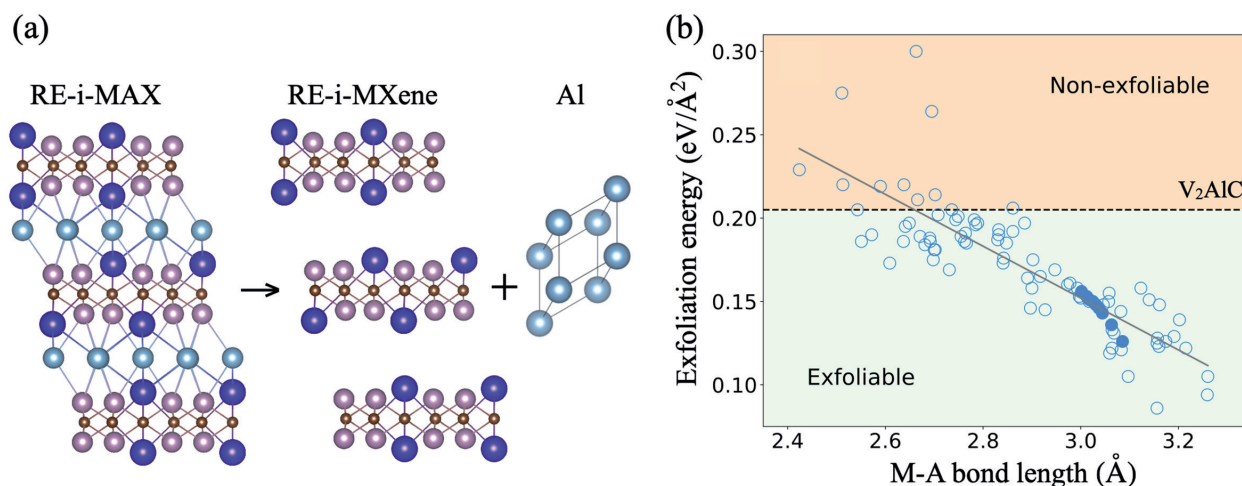


Figure 12. (a) Simplified representation of the exfoliation of a RE-i-MAX phase into RE-i-MXene, for which the exfoliation energy is obtained as a difference in energy of the products (RE-i-MXene + Al) and the reactant (RE-i-MAX). (b) Computed static exfoliation energy as a function of the bond length for a series of 82 MAX phases (empty markers) [116] plus the 9 considered RE-i-MAX phases (full markers).

5.4. Conclusions

In summary, we reported on the growth and characterization of nine representative members of the new family of RE-i-MAX single crystals, *viz.* $(\text{Mo}_{2/3}\text{RE}_{1/3})_2\text{AlC}$ with RE = Nd, Sm, Gd, Tb, Dy, Ho, Er, Tm, and Lu. Their structures and elastic properties were addressed and their exfoliation

potential into 2D RE-i-MXenes was predicted, via a complete analysis of both bond strengths and exfoliation energies. Overall, we believe that the theoretical prediction of the exfoliation potential of the RE-i-MAX phases represents a promising breakthrough for future experimental exfoliation of these systems, and their potential use in applications where 2D magnetic materials are desired.

6. Investigation of V_2CT_2 MXenes

Since the discovery of the first MXene less than 10 years ago, remarkable progress has been made in the synthesis process, in the characterization of the structural and physical properties, and in the search for potential applications. However, among the several dozens of MXenes predicted to date, the first reported $Ti_3C_2T_z$ system has attracted most attention, with about half of the works dedicated to it.

In the context of this thesis, we decided to focus on the vanadium-based MXenes and to investigate the structural, electronic, and vibrational properties of both pristine V_2C and terminated V_2CT_z ($T = F, OH$) monolayers using first-principles techniques.

6.1. Structural properties

The ground state structure of the pristine V_2C with fully relaxed geometry is found to be hexagonal. The unit cell includes three atoms, two V and one C, and resides in the $p\bar{3}m1$ (#164) space group. The atoms are therefore arranged in a triple-layer structure where the C layer is sandwiched between the two V layers (Figure 13(a)). The lattice constant a is equal to 2.89 Å, and the layer thickness d equals 2.18 Å.

Based on the unit cell of pristine V_2C , functionalized V_2CT_2 structures were constructed. Depending on the relative positions of the terminal groups, different functionalization models can be built (Figures 13(b)–13(e)) [52]. Given that the properties of MXenes can strongly vary with the nature and position of the terminal groups, it was mandatory to systematically investigate all possible configurations and evaluate their respective stability. For this purpose, the formation energies of all configurations were computed. It was found that the energetically favored structures for V_2C -based systems functionalized with $-F$ and $-OH$ groups corresponded to MD2 model, where the terminal groups occupy fcc sites (Figure 13(c)) [122].

6.2. Electronic properties

According to its electronic band structure, the V_2C monolayer exhibits a metallic behavior (Figure 14(a)). In contrast with the well-studied Ti_3C_2 MXene system which undergoes a metallic to indirect band gap semiconductor transition [123], the V_2C system preserved its metallic character upon functionalization (Figures 14(b)–14(d)) [122].

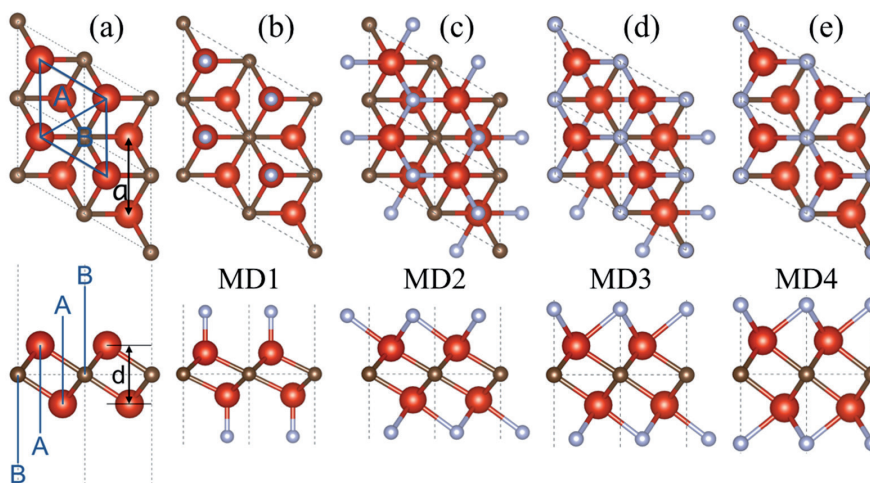


Figure 13. Atomic structures of (a) pristine V_2C and four models for terminated V_2CT_2 : (b) MD1, (c) MD2, (d) MD3, and (e) MD4 - top and side views. V and C atoms are respectively in red and brown, while the functional groups ($T = F, OH$) are in blue. In (a), a and d are the lattice constant and the layer thickness, respectively.

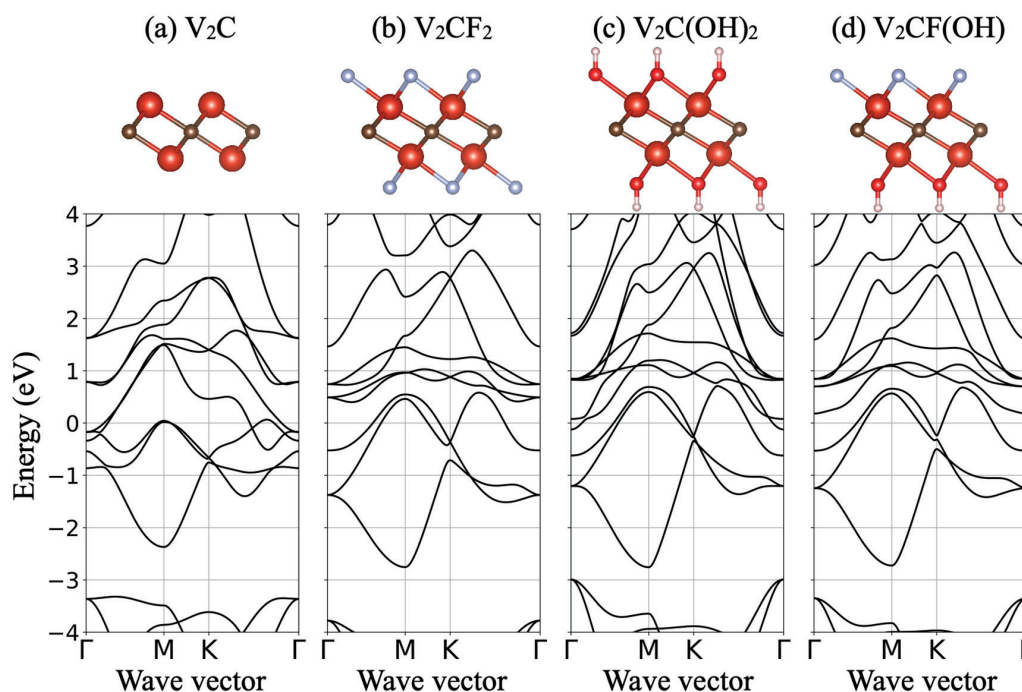


Figure 14. Electronic band structure of (a) V_2C , (b) V_2CF_2 , (c) $V_2C(OH)_2$, and (d) $V_2CF(OH)$ in their high-symmetric configuration. The Fermi level is fixed as the reference of zero energy.

6.3. Vibrational properties

Thanks to its sensitivity to very small changes in crystal structures, Raman spectroscopy is usually used to characterize the composition and the quality of samples. However, before it can be used for this purpose, it is fundamental to properly define the peak positions and to assign them to the computed vibrational modes. This allows to identify the contribution of each atom and group of atoms in the various vibrational modes corresponding to the reported peaks.

In this context, the phonon mode frequencies of both pristine V_2C and terminated V_2CT_2 systems were computed from first-principles. Making good use of the group theory, the Raman and infrared activity of the modes was predicted. A total of 2, 4, 6, and 10 Raman-active modes were predicted, respectively for the V_2C , V_2CF_2 , $V_2C(OH)_2$, and $V_2CF(OH)$ systems.

The experimental Raman spectrum of a V_2C -based sample is presented in Figure 15 (solid black line). As a global observation, the peaks

were relatively broad which may be due to substantial defects concentrations.

The calculated Raman-active frequencies of all V_2C -based systems are reported under the experimental spectrum (Figure 15). The predicted peak positions for the V_2C monolayer were not sufficient to describe the experimental Raman spectrum, especially above 400 cm^{-1} and $-OH$ groups, additional Raman frequencies appeared around 520 cm^{-1} and around 440 and 530 cm^{-1} , respectively. However, there were still some discrepancies between the theoretical predictions and the experimental spectrum, as some predicted frequencies did not correspond to any Raman bands and vice versa. Eventually, considering the heterogeneously-terminated $V_2CF(OH)$ monolayer, several additional Raman-active modes appeared between 430 and 760 cm^{-1} , which matched well with the bands around 430 and 520 cm^{-1} and with the hump centered at 650 cm^{-1} in the experimental spectrum. This close matching between the theoretically predicted positions of the Raman-active peaks and the experimental Raman spectrum reflected the fact that the ter-

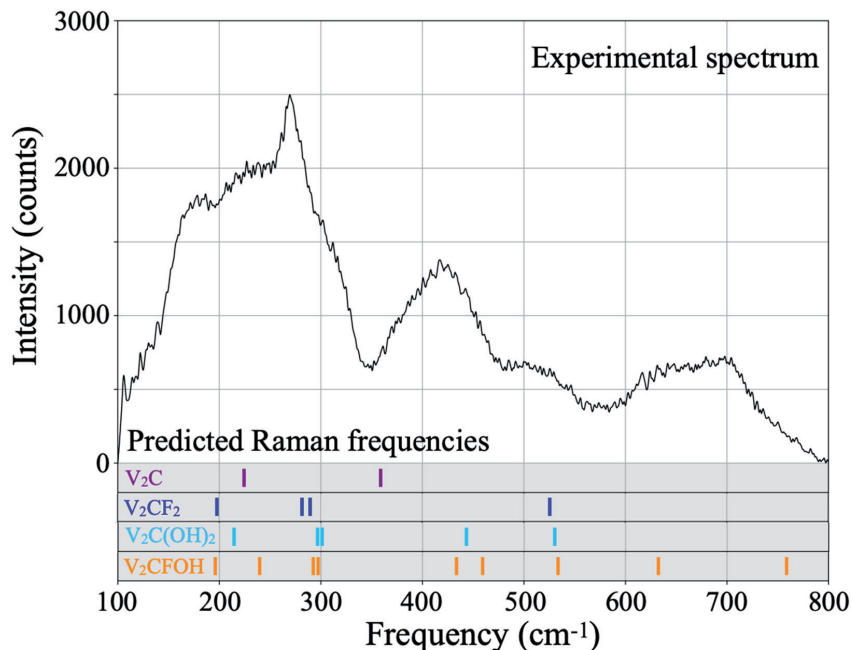


Figure 15. Raman spectrum of the exfoliated V_2C -based sample collected at RT. The calculated Raman-active frequencies of the V_2C , V_2CF_2 , $V_2C(OH)_2$, and V_2CFOH mono-sheets are included under the experimental spectrum for comparison. The matching between the predicted normal-mode frequencies and the experimental spectrum confirms the presence of heterogeneous terminal groups at the V_2C surface.

minal groups were actually heterogeneous and most likely randomly distributed at the V_2C surface [122].

6.4. Conclusions

In conclusion, the static and dynamical properties of pristine bare V_2C and terminated V_2CT_2 ($T = F$ and OH) monolayers have been investigated using first-principles and experimental techniques. In particular, the comparison of our theoretical predictions with the experimental Raman spectrum gave a relatively good agreement, especially when considering mixed terminal groups at the MXenes surface.

7. Conclusions

With roughly 2,000 publications on the MAX phases, and over 2,300 ones on the MXenes, it is clear that both MAX and MXenes have considerably attracted and are still attracting attention from the scientific community. Without exception, our group has jumped into this exciting

field and, during four years, I have been fortunate to work on MAX phases and MXenes.

In summary, this thesis has been devoted to the investigation of the structural, electronic, vibrational, thermal, and elastic properties of the 3D MAX phase single crystals and the derived 2D MXenes. The approach adopted throughout these four years consisted in a subtle combination of theoretical predictions and experimental measurements. Among others, this work allowed to gain insight into the anisotropy present in the MAX phase properties, to understand the bonding nature and strength within quaternary RE-i-MAX phases, and to predict their potential exfoliation into RE-i-MXenes. Additionally, the electronic and vibrational properties of V_2CT_z MXenes functionalized either with homogeneous or heterogeneous terminal groups have been studied theoretically and compared to experimental measurements. This led to the main conclusion that heterogeneous terminal groups must be considered in the calculations in order to more accurately reproduce the experimental conditions and recover the experimental results.

Acknowledgments

The author acknowledges financial support from Wallonie-Bruxelles-International and from the Fédération Wallonie-Bruxelles through the Action de Recherche Concertée (ARC) on 3D nanoarchitecturing of 2D crystals (No. 16/21-077). The author is also indebted to the Flag-ERA JTC 2017 project entitled "MORE-MXenes". Computational resources were provided by the supercomputing facilities of the UCLouvain (CISM) and the Consortium des Equipements de Calcul Intensif en Fédération Wallonie-Bruxelles (CECI) funded by the Fonds de la Recherche Scientifique de Belgique (F.R.S.- FNRS) under convention No. 2.5020.11.

References

- [1] M. W. Barsoum, *Progress in Solid State Chemistry* 28, 201 (2000).
- [2] M. Naguib, M. Kurtoglu, V. Presser, J. Lu, J. Niu, M. Heon, L. Hultman, Y. Gogotsi, and M. W. Barsoum, *Advanced Materials* 23, 4248 (2011).
- [3] M. Naguib, V. N. Mochalin, M. W. Barsoum, and Y. Gogotsi, *Advanced Materials* 26, 992 (2014).
- [4] M. W. Barsoum, *MAX Phases*, 1st ed. (Wiley-Blackwell, 2013).
- [5] V. H. Nowotny, *Progress in Solid State Chemistry* 5, 27 (1971).
- [6] W. Jeitschko and H. Nowotny, *Monatsh. Chem.* 98, 329 (1967).
- [7] H. Wolfsgruber, H. Nowotny, and F. Benesovsky, *Monatsh. Chem.* 98, 2403 (1967).
- [8] M. A. Pietzka and S. J., *Journal of Phase Equilibria* 15, 392 (1994).
- [9] M. A. Pietzka and S. J., *Journal of the American Ceramic Society* 79, 2321 (1996).
- [10] J. Schuster and H. Nowotny, *Zeitschrift fuer Metallkunde* 71, 341 (1980).
- [11] M. W. Barsoum and T. El-Raghy, *Journal of the American Ceramic Society* 79, 1953 (1996).
- [12] M. W. Barsoum, D. Brodtkin, and T. El-Raghy, *Scripta Materialia* 36, 535 (1997).
- [13] M. W. Barsoum, L. Farber, I. Levin, A. Procopio, T. El-Raghy, and A. Berner, *Journal of the American Ceramic Society* 82, 2545 (1999).
- [14] M. W. Barsoum, T. El-Raghy, and A. Procopio, *Metallurgical and Materials Transactions A* 31, 333 (2000).
- [15] F. Mercier, T. Ouisse, and D. Chaussende, *Phys. Rev. B* 83, 075411 (2011).
- [16] F. Mercier, O. Chaix-Pluchery, T. Ouisse, and D. Chaussende, *Applied Physics Letters* 98, 081912 (2011).
- [17] F. Meng, Y. Zhou, and J. Wang, *Scripta Materialia* 53, 1369 (2005).
- [18] T. Cabioch, P. Eklund, V. Mauchamp, M. Jaouen, and M. W. Barsoum, *Journal of the European Ceramic Society* 33, 897 (2013).
- [19] A. Mockute, J. Lu, E. J. Moon, M. Yan, B. Anasori, S. J. May, M. W. Barsoum, and J. Rosen, *Materials Research Letters* 3, 16 (2015).
- [20] Z. Liu, E. Wu, J. Wang, Y. Qian, H. Xiang, X. Li, Q. Jin, G. Sun, X. Chen, J. Wang, and M. Li, *Acta Materialia* 73, 186 (2014).
- [21] E. N. Caspi, P. Chartier, F. Porcher, F. Damay, and T. Cabioch, *Materials Research Letters* 3, 100 (2015).
- [22] B. Anasori, Y. Xie, M. Beidaghi, J. Lu, B. C. Hosler, L. Hultman, P. R. C. Kent, Y. Gogotsi, and M. W. Barsoum, *ACS Nano* 9, 9507 (2015).
- [23] R. Meshkian, M. Dahlqvist, J. Lu, B. Wickman, J. Halim, J. Thrnberg, Q. Tao, S. Li, S. Intikhab, J. Snyder, M. W. Barsoum, M. Yildizhan, J. Palisaitis, L. Hultman, P. O. A. Persson, and J. Rosen, *Advanced Materials* 30, 1706409 (2018).
- [24] Q. Tao, M. Dahlqvist, J. Lu, S. Kota, R. Meshkian, J. Halim, J. Palisaitis, L. Hultman, M. W. Barsoum, P. O. A. Persson, and J. Rosen, *Nature Communications* 8, 1 (2017).
- [25] M. Dahlqvist, J. Lu, R. Meshkian, Q. Tao, L. Hultman, and J. Rosen, *Science Advances* 3, 1 (2017).
- [26] J. Lu, A. Thore, R. Meshkian, Q. Tao, L. Hultman, and J. Rosen, *Crystal Growth & Design* 17, 5704 (2017).
- [27] M. Dahlqvist, A. Petruhins, J. Lu, L. Hultman, and J. Rosen, *ACS Nano* 12, 7761 (2018).
- [28] L. Chen, M. Dahlqvist, T. Lapauw, B. Tunca, F. Wang, J. Lu, R. Meshkian, K. Lambrinou, B. Blanpain, J. Vleugels, and J. Rosen, *Inorganic Chemistry* 57, 6237 (2018).
- [29] A. Petruhins, M. Dahlqvist, J. Lu, L. Hultman, and J. Rosen, *Crystal Growth & Design* 20, 55 (2020).
- [30] Q. Tao, J. Lu, M. Dahlqvist, A. Mockute, S. Calder, A. Petruhins, R. Meshkian, O. Rivin, D. Potashnikov, E. Caspi, H. Shaked, A. Hoser, C. Opagiste, R.-M. Galera, R. Salikhov, U. Wiedwald, C. Ritter, A. R. Wildes, B. Johansson, L. Hultman, M. Farle, M. W. Barsoum, and J. Rosen, *Chemistry of Materials* 31, 2476 (2019).
- [31] A. Petruhins, J. Lu, L. Hultman, and J. Rosen, *Materials Research Letters* 7, 446 (2019).
- [32] Q. Tao, T. Ouisse, D. Pinek, O. Chaix-Pluchery, F. Wilhelm, A. Rogalev, C. Opagiste, L. Jouffret, A. Champagne, J.-C. Charlier, J. Lu, L. Hultman, M. W. Barsoum, and J. Rosen, *Phys. Rev. Materials* 2, 114401 (2018).
- [33] M. Sokol, V. Natu, S. Kota, and M. W. Barsoum, *Trends in Chemistry* 1, 210 (2019).
- [34] M. W. Barsoum and T. El-Raghy, *American Scientist* 89, 334 (2001).
- [35] M. Nelson, M. T. Agne, B. Anasori, J. Yang, and M. W. Barsoum, *Materials Science and Engineering: A* 705, 182 (2017).
- [36] X. Wang and Y. Zhou, *Journal of Materials Science & Technology* 26, 385 (2010).
- [37] A. S. Ingason, A. Mockute, M. Dahlqvist, F. Magnus, S. Olafsson, U. B. Arnalds, B. Alling, I. A. Abrikosov, B. Hjörvarsson, P. O. A. Persson, and J. Rosen, *Phys. Rev. Lett.* 110, 195502 (2013).
- [38] A. S. Ingason, M. Dahlqvist, and J. Rosen, *Journal of Physics: Condensed Matter* 28, 433003 (2016).
- [39] S. E. Lofland, J. D. Hettinger, K. Harrell, P. Finkel, S. Gupta, M. W. Barsoum, and G. Hug, *Applied Physics Letters* 84, 508 (2004).

- [40] J. D. Hettinger, S. E. Lofland, P. Finkel, T. Meehan, J. Palma, K. Harrell, S. Gupta, A. Ganguly, T. El-Raghy, and M. W. Barsoum, *Phys. Rev. B* 72, 115120 (2005).
- [41] L. Verger, C. Xu, V. Natu, H.-M. Cheng, W. Ren, and M. W. Barsoum, *Oxidation of Metals* 59, 303 (2019).
- [42] M. Sundberg, G. Malmqvist, A. Magnusson, and T. El-Raghy, *Ceramics International* 30, 1899 (2004), 3rd Asian Meeting on Electroceramics.
- [43] J. W. Byeon, J. Liu, M. Hopkins, W. Fischer, N. Garimella, K. B. Park, M. P. Brady, M. Radovic, T. El-Raghy, and Y. H. Sohn, *Oxidation of Metals* 68, 97 (2007).
- [44] Z. Lin, M. Li, J. Wang, and Y. Zhou, *Scripta Materialia* 58, 29 (2008).
- [45] S. Basu, N. Obando, A. Gowdy, I. Karaman, and M. Radovic, *Journal of The Electrochemical Society* 159, C90 (2011).
- [46] D. J. Tallman, B. Anasori, and M. W. Barsoum, *Materials Research Letters* 1, 115 (2013).
- [47] M. Haftani, M. S. Heydari, H. R. Baharvandi, and N. Ehsani, *International Journal of Refractory Metals and Hard Materials* 61, 51 (2016).
- [48] K. S. Novoselov, A. K. Geim, S. V. Morozov, D. Jiang, Y. Zhang, S. V. Dubonos, I. V. Grigorieva, and A. A. Firsov, *Science* 306, 666 (2004).
- [49] K. S. Novoselov, A. K. Geim, S. V. Morozov, D. Jiang, M. I. Katsnelson, I. V. Grigorieva, S. V. Dubonos, and A. A. Firsov, *Nature* 438, 197 (2005).
- [50] M. Naguib, O. Mashtalir, J. Carle, V. Presser, J. Lu, L. Hultman, Y. Gogotsi, and M. W. Barsoum, *Acs Nano* 6, 1322 (2012).
- [51] B. Anasori and Y. Gogotsi, *2D Metal Carbides and Nitrides (MXenes)*, 1st ed. (Springer International Publishing, 2019).
- [52] M. Khazaei, M. Arai, T. Sasaki, C.-Y. Chung, N. S. Venkataramanan, M. Estili, Y. Sakka, and Y. Kawazoe, *Advanced Functional Materials* 23, 2185 (2013).
- [53] I. Persson, A. el Ghazaly, Q. Tao, J. Halim, S. Kota, V. Darakchieva, J. Palisaitis, M. W. Barsoum, J. Rosen, and P. O. A. Persson, *Small* 14, 1703676 (2018).
- [54] M. Khazaei, A. Mishra, N. S. Venkataramanan, A. K. Singh, and S. Yunoki, *Current Opinion in Solid State and Materials Science* 23, 164 (2019).
- [55] C. Si, J. Zhou, and Z. Sun, *ACS Applied Materials & Interfaces* 7, 17510 (2015).
- [56] M. Khazaei, V. Wang, C. Sevik, A. Ranjbar, M. Arai, and S. Yunoki, *Phys. Rev. Materials* 2, 074002 (2018).
- [57] A. Champagne and J.-C. Charlier, *Journal of Physics: Materials* 3, 032006 (2020).
- [58] H. Kumar, N. C. Frey, L. Dong, B. Anasori, Y. Gogotsi, and V. B. Shenoy, *ACS Nano* 11, 7648 (2017).
- [59] G. Wang, *The Journal of Physical Chemistry C* 120, 18850 (2016).
- [60] J. He, P. Lyu, and P. Nachtigall, *J. Mater. Chem. C* 4, 11143 (2016).
- [61] M. Kurtoglu, M. Naguib, Y. Gogotsi, and M. W. Barsoum, *MRS Communications* 2, 133 (2012).
- [62] N. Zhang, Y. Hong, S. Yazdanparast, and M. A. Zaeem, *2D Materials* 5, 045004 (2018).
- [63] X.-H. Zha, K. Luo, Q. Li, Q. Huang, J. He, X. Wen, and S. Du, *Europhysics Letters* 111, 26007 (2015).
- [64] V. N. Borysiuk, V. N. Mochalin, and Y. Gogotsi, *Nanotechnology* 26, 265705 (2015).
- [65] A. Lipatov, H. Lu, M. Alhabeb, B. Anasori, A. Gruverman, Y. Gogotsi, and A. Sinitkii, *Science Advances* 4, 1 (2018).
- [66] M. R. Lukatskaya, S. Kota, Z. Lin, M.-Q. Zhao, N. Shpigel, M. D. Levi, J. Halim, P.-L. Taberna, M. W. Barsoum, P. Simon, and Y. Gogotsi, *Nature Energy* 2, 17105 (2017).
- [67] G. Ying, A. D. Dillon, A. T. Fafarman, and M. W. Barsoum, *Materials Research Letters* 5, 391 (2017).
- [68] G. Ying, S. Kota, A. D. Dillon, A. T. Fafarman, and M. W. Barsoum, *FlatChem* 8, 25 (2018).
- [69] F. Shahzad, M. Alhabeb, C. B. Hatter, B. Anasori, S. Man Hong, C. M. Koo, and Y. Gogotsi, *Science* 353, 1137 (2016).
- [70] M. R. Lukatskaya, B. Dunn, and Y. Gogotsi, *Nature Communications* 7, 1 (2016).
- [71] Q. Hu, D. Sun, Q. Wu, H. Wang, L. Wang, B. Liu, A. Zhou, and J. He, *Journal of Physical Chemistry A* 117, 14253 (2013).
- [72] Q. Hu, H. Wang, Q. Wu, X. Ye, A. Zhou, D. Sun, L. Wang, B. Liu, and J. He, *International Journal of Hydrogen Energy* 39, 10606 (2014).
- [73] J. Pang, R. G. Mendes, A. Bachmatiuk, L. Zhao, H. Q. Ta, T. Gemming, H. Liu, Z. Liu, and M. H. Rummeli, *Chem. Soc. Rev.* 48, 72 (2019).
- [74] X.-f. Yu, Y.-c. Li, J.-b. Cheng, Z.-b. Liu, Q.-z. Li, W.-z. Li, X. Yang, and B. Xiao, *ACS Applied Materials & Interfaces* 7, 13707 (2015).
- [75] H. Liu, C. Duan, C. Yang, W. Shen, F. Wang, and Z. Zhu, *Sensors and Actuators B: Chemical* 218, 60 (2015).
- [76] G. Liu, J. Shen, Q. Liu, G. Liu, J. Xiong, J. Yang, and W. Jin, *Journal of Membrane Science* 548, 548 (2018).
- [77] M. Khazaei, M. Arai, T. Sasaki, M. Estili, and Y. Sakka, *Phys. Chem. Chem. Phys.* 16, 7841 (2014).
- [78] A. N. Gandhi, H. N. Alshareef, and U. Schwingenschlgl, *Chemistry of Materials* 28, 1647 (2016).
- [79] S. Kumar and U. Schwingenschlgl, *Phys. Rev. B* 94, 035405 (2016).
- [80] X.-H. Zha, Q. Huang, J. He, H. He, J. Zhai, J. S. Francisco, and S. Du, *Scientific Reports* 6, 27971 (2016).
- [81] Z. Ling, C. E. Ren, M.-Q. Zhao, J. Yang, J. M. Giammarco, J. Qiu, M. W. Barsoum, and Y. Gogotsi, *Proceedings of the National Academy of Sciences* 111, 16676 (2014).
- [82] X. Xie, Y. Xue, L. Li, S. Chen, Y. Nie, W. Ding, and Z. Wei, *Nanoscale* 6, 11035 (2014).
- [83] Z. W. Seh, K. D. Fredrickson, B. Anasori, J. Kibsgaard, A. L. Strickler, M. R. Lukatskaya, Y. Gogotsi, T. F. Jaramillo, and A. Vojvodic, *ACS Energy Letters* 1, 589 (2016).
- [84] H. Wang, Y. Wu, X. Yuan, G. Zeng, J. Zhou, X. Wang, and J. W. Chew, *Advanced Materials* 30, 1704561 (2018).
- [85] O. Mashtalir, K. M. Cook, V. N. Mochalin, M. Crowe, M. W. Barsoum, and Y. Gogotsi, *J. Mater. Chem. A* 2, 14334 (2014).
- [86] Y. Liu, Q. Tao, Y. Jin, X. Liu, H. Sun, A. E. Ghazaly, S. Fabiano, Z. Li, J. Luo, J. Rosen, and F. Zhang, *ACS Applied Electronic Materials* 2, 163 (2020).
- [87] L. Qin, J. Jiang, Q. Tao, C. Wang, I. Persson, M. Fahlman, P. O. A. Persson, L. Hou, J. Rosen, and F. Zhang, *J. Mater. Chem. A* 8, 5467 (2020).
- [88] M. K. Drulis, H. Drulis, S. Gupta, M. W. Barsoum, and T. El-Raghy, *Journal of Applied Physics* 99, 093502 (2006).
- [89] T. Ouisse, E. Sarigiannidou, O. Chaix-Pluchery, H. Roussel, B. Doisneau, and D. Chaussende, *Journal of Crystal Growth* 384, 88 (2013).
- [90] L. Shi, T. Ouisse, E. Sarigiannidou, O. Chaix-Pluchery, H. Roussel, D. Chaussende, and B. Hackens, *Acta Materialia* 83, 304 (2015).

- [91] T. Ouisse, L. Shi, B. A. Piot, B. Hackens, V. Mauchamp, and D. Chaussende, *Phys. Rev. B* 92, 045133 (2015).
- [92] T. Ouisse and M. W. Barsoum, *Materials Research Letters* 5, 365 (2017).
- [93] T. Ito, D. Pinek, T. Fujita, M. Nakatake, S.-i. Ideta, K. Tanaka, and T. Ouisse, *Phys. Rev. B* 96, 195168 (2017).
- [94] S. Baroni, P. Giannozzi, and A. Testa, *Phys. Rev. Lett.* 58, 1861 (1987).
- [95] X. Gonze, *Phys. Rev. A* 52, 1086 (1995).
- [96] X. Gonze, *Phys. Rev. B* 55, 10337 (1997).
- [97] X. Gonze and C. Lee, *Phys. Rev. B* 55, 10355 (1997).
- [98] S. Baroni, S. de Gironcoli, A. Dal Corso, and P. Giannozzi, *Rev. Mod. Phys.* 73, 515 (2001).
- [99] A. Champagne, F. Bourdarot, P. Bourges, P. Piekarczyk, D. Pinek, I. Glard, J.-C. Charlier, and T. Ouisse, *Materials Research Letters* 6, 378 (2018).
- [100] A. Champagne, J.-L. Battaglia, T. Ouisse, F. Ricci, A. Kusiak, C. Pradere, V. Natu, A. Dewandre, M. J. Verstraete, M. W. Barsoum, J.-C. Charlier, *Journal of Physical Chemistry C* 124, 24017 (2020).
- [101] M. Kawamura, *Computer Physics Communications* 239, 197 (2019).
- [102] G. K. Madsen and D. J. Singh, *Computer Physics Communications* 175, 67 (2006).
- [103] G. K. Madsen, J. Carrete, and M. J. Verstraete, *Computer Physics Communications* 231, 140 (2018).
- [104] O. Hellman, I. A. Abrikosov, and S. I. Simak, *Phys. Rev. B* 84, 180301 (2011).
- [105] O. Hellman, P. Steneteg, I. A. Abrikosov, and S. I. Simak, *Phys. Rev. B* 87, 104111 (2013).
- [106] O. Hellman and I. A. Abrikosov, *Phys. Rev. B* 88, 144301 (2013).
- [107] A. Kusiak, J. Martan, J.-L. Battaglia, and R. Daniel, *Thermochimica Acta* 556, 1 (2013).
- [108] E. Ruffio, C. Pradere, A. Sommier, J.-C. Batsale, A. Kusiak, and J.-L. Battaglia, *International Journal of Thermal Sciences* 129, 385 (2018).
- [109] W. C. Oliver and G. M. Pharr, *Journal of Materials Research* 7, 1564 (1992).
- [110] I. C. Albayrak, S. Basu, A. Sakulich, O. Yehekel, and M. W. Barsoum, *Journal of the American Ceramic Society* 93, 2028 (2010).
- [111] H. O. Badr, A. Champagne, T. Ouisse, J.-C. Charlier, and M. W. Barsoum, *Phys. Rev. Materials* 4, 083605 (2020).
- [112] M. Barsoum and G. Tucker, *Scripta Materialia* 139, 166 (2017).
- [113] M. W. Barsoum, X. Zhao, S. Shanazarov, A. Romanchuk, S. Koumlis, S. J. Pagano, L. Lamberson, and G. J. Tucker, *Phys. Rev. Materials* 3, 013602 (2019).
- [114] A. Champagne, O. Chaix-Pluchery, T. Ouisse, D. Pinek, I. G elard, L. Jouffret, M. Barbier, F. Wilhelm, Q. Tao, J. Lu, J. Rosen, M. W. Barsoum, and J.-C. Charlier, *Phys. Rev. Materials* 3, 053609 (2019).
- [115] A. Champagne, F. Ricci, M. Barbier, T. Ouisse, D. Magnin, S. Ryelandt, T. Pardoën, G. Hautier, M. W. Barsoum, and J.-C. Charlier, *Phys. Rev. Materials* 4, 013604 (2020).
- [116] M. Khazaei, A. Ranjbar, K. Esfarjani, D. Bogdanovski, R. Dronskowski, and S. Yunoki, *Phys. Chem. Chem. Phys.* 20, 8579 (2018).
- [117] M. Khazaei, J. Wang, M. Estili, A. Ranjbar, S. Suehara, M. Arai, K. Esfarjani, and S. Yunoki, *Nanoscale* 11, 11305 (2019).
- [118] R. Dronskowski and P. E. Bloechl, *The Journal of Physical Chemistry* 97, 8617 (1993).
- [119] V. L. Deringer, A. L. Tchougreff, and R. Dronskowski, *The Journal of Physical Chemistry A* 115, 5461 (2011).
- [120] S. Maintz, V. L. Deringer, A. L. Tchougreff, and R. Dronskowski, *Journal of Computational Chemistry* 34, 2557 (2013).
- [121] M. Dahlqvist and J. Rosen, *Phys. Chem. Chem. Phys.* 17, 31810 (2015).
- [122] A. Champagne, L. Shi, T. Ouisse, B. Hackens, and J.-C. Charlier, *Phys. Rev. B* 97, 115439 (2018).
- [123] T. Hu, J. Wang, H. Zhang, Z. Li, M. Hu, and X. Wang, *Phys. Chem. Chem. Phys.* 17, 9997 (2015).